Fractal radar scattering from soil

Klaudia Oleschko,[1,*] Gabor Korvin,[2] Benjamin Figueroa,[3] Marco Antonio Vuelvas,[4] Alexander S. Balankin,[5] Lourdes Flores,[1] and Dora Carreón[1]

[1]*Instituto de Geologia, Universidad Nacional Autónoma de México (UNAM), Ciudad Universitaria, Apartado Postal 70-296, CP 04510, Coyoacan, México, Distrito Federal, Mexico*

[2]*King Fahd University of Petroleum and Minerals, Dhahran 31261, Saudi Arabia*

[3]*Colegio de Postgraduados, km.35.5 Carretera México–Texcoco, Montecillo, Estado de México, CP 56230, Mexico*

[4]*Instituto Nacional de las Investigaciones Forestales y Agropecuárias (INIFAP), km.6.5 Carretera Celaya–San Miguel Allende, Celaya, Guanajuato 38001, Mexico*

[5]*SEPI-ESIME, Edificio 5, 3er Piso, Instituto Politécnico Nacional, México, Distrito Federal 07738, Mexico*

A general technique is developed to retrieve the fractal dimension of self-similar soils through microwave (radar) scattering. The technique is based on a mathematical model relating the fractal dimensions of the georadargram to that of the scattering structure. Clear and different fractal signatures have been observed over four geosystems (soils and sediments) compared in this work.

I. INTRODUCTION

Wave scattering on fractal refractive index fluctuations and on fractal surfaces has found applications in all fields of science to characterize the irregular geometry of surfaces and volumes [1–4]. The use of small-angle x ray and neutron scattering and optical diffraction has made it possible to determine the fractal dimension of different mass and surface fractals over ten decades of length scales [5–8]. Electromagnetic scattering was also proposed to retrieve a typical dimension for multiscale surfaces [2,6,9–11].

The nonuniform internal structure of an R-sized fractal aggregate in the E-dimensional space manifests itself in nontrivial mass M and density ρ scaling [12]

$$M \propto m_0 (R/a_0)^D, \tag{1.1}$$

and

$$\rho \propto \rho_0 (R/a_0)^{D-E}, \tag{1.2}$$

where D is mass fractal dimension, m_0, ρ_0, and a_0 are mass, density, and size of the constituent particles, respectively. Their density correlation function $C(\vec{R}) \propto \langle \rho(\vec{r}+\vec{R})\rho(\vec{r}) \rangle$ scales as

$$C(\vec{R}) \propto R^{D-E}. \tag{1.3}$$

The intensity of monochromatic waves scattered on the mass fractal is proportional to

$$S(\vec{q}) = \int \int d\vec{x} \, d\vec{x}' \, C(\vec{x}-\vec{x}') \exp[i\vec{q} \cdot (\vec{x}-\vec{x}')], \tag{1.4}$$

where $\vec{q}$ is the wave vector. From Eqs. (1.3) and (1.4)

$$S(\vec{q}) \sim |\vec{q}|^{-D}. \tag{1.5}$$

If the scattering takes place on fluctuations of the refractive index r,

$$S(\vec{q}) \propto \int \langle r(\vec{x}') \cdot r(x+\vec{x}') \rangle \exp(-i\vec{q} \cdot \vec{x}) dV. \tag{1.6}$$

As the correlation function of the refractive index fluctuations is proportional to that of the material density $\rho(\vec{x})$ [12], we have in this case as well $S(\vec{q}) \sim |\vec{q}|^{-D}$. Small angle x-ray, neutron, or optical scattering measurements use Eq. (1.5) to determine the fractal dimension of aerogels, colloidal aggregates, and polymers. These techniques cannot be applied *in situ* to natural fractals, as for instance soils.

Most theoretical work have been done in Fourier domain, but since Berry's [13] "diffractal" theory there have been attempts [4,13–15] to infer the fractal dimension of the scatterer from the time history of the scattered pulses. However, ground penetration radar (GPR [16,17]) has apparently never been used for this type of research.

In this work, we developed a mathematical model, a wave simulation software, and a fractal analysis technique to retrieve the dimensionality of fractally porous systems through microwave scattering. With these techniques, we analyzed GPR georadargrams recorded over different soils and sediments of Mexico, previously documented isotropic mass fractals in the 0.009–0.2 cm range [18].

II. TIME-DOMAIN ASPECTS OF FRACTAL SCATTERING

Instead of the Fourier representation (1.4) and (1.5), we shall study the scattering process as it evolves in time [4,19]. A simple time-domain argument shows that the backscattered pulse train is fractal, and its fractal dimension is related to that of the scatterer.

Suppose we send a narrow-band signal $s(t)$ into a soil section, between depths $z=0$ and $z=Z_{max}$. Let the transmit-

―――――
*Corresponding author.
Email address: olechko@servidor.unam.mx

ter and receiver antennas be at $x=0$, $z=0$. Neglecting multiples, the received signal is

$$A(t) \propto \sum_{j=1}^{N \gg 1} I_j(\vec{q}_j) n_j(\vec{q}_j) e^{i\vec{q}_j ct}, \qquad (2.1)$$

where $I_j(\vec{q}_j)$ is the intensity of the wave scattered from a volume element with scattering vector $\vec{q}_j$, $n_j(\vec{q}_j)$ is the number of discrete scatterers having the same scattering vector, and c is electromagnetic (em) wave speed in soil. By Hunt's [20] theorem, *if* $A_j(\vec{q}_j) = I_j(\vec{q}_j) n_j(\vec{q}_j)$ *satisfies the conditions*
  (i) $a|\vec{q}_j| \leq |\vec{q}_{j+1}| \leq b|\vec{q}_j|$ *for some* $b > a > 1$ *and for all* j,
  (ii) $-1 < \lim_{j \to \infty} \ln A_j / \ln|\vec{q}_j| = -H < 0$, *then the wave amplitude* $A(t)$ *[given by Eq. (2.1)] is a self-affine generalized Weierstrass function* [15,21–24], *the self-affinity dimension of the graph of* $A(t)$ *is* $2-H$, *and the trace of* $A(t)$ *has a Hausdorff dimension* $D = 2-H$. To check the fulfillment of conditions (i) and (ii), assume that all backscattered energy comes from the plane of measurement. Then

$$n_j(\vec{q}_j) \propto |\vec{q}_j|^D, \qquad (2.2)$$

where D is mass fractal dimension of the scatterers ($1 \leq D \leq 2$). As the scatterers are randomly oriented two-dimensional objects (platelets of clay minerals, layer-wise deposited grains, cracks, layer boundaries), the scattering intensity from a single scatterer scales as

$$I_j(\vec{q}_j) \propto |\vec{q}_j|^{-2} \qquad (2.3)$$

[25]. In fractal soil, both the grain-size and pore-size distributions consist of a finite number of geometrically decreasing size classes [26]. Radar only penetrates a limited range, so there are only a finite number of different scattering vectors $\vec{q}_j$. Consequently, some constants a and b can be found to satisfy condition (i). By Eqs. (2.2) and (2.3)

$$A_j(\vec{q}_j) = I_j(\vec{q}_j) n_j(\vec{q}_j) \propto |\vec{q}_j|^{D-2}, \qquad (2.4)$$

and taking the limit in condition (ii) gives

$$-1 < \lim_{j \to \infty} \frac{\ln A_j}{\ln|\vec{q}_j|} = D - 2 < 0, \qquad (2.5)$$

proving that the graph of $A(t)$ has the same fractal dimension D as the mass fractal dimension of the soil's scatterers. Sections II A and II B and the Appendix will develop this heuristic argument to a convolutional model.

A. Convolutional model of radar wave reflection from soil

Geophysical fields are fractals [21–24]. The self-similar or self-affine nature of magnetic susceptibility, albedo, brightness, temperature, topography, and other fields [27–31] is well documented. The fractal dimension of these fields must be known when designing a measuring network, otherwise small fractal dimensional anomalies will be lost [22,31–33].

We consider common offset or common depth point georadargrams [16]. Because of attenuation [34], only reflec-

tions from not deeper than a few times the dominant wavelength are recorded. Assume the input $s(t)$ has *Dirac-δ* autocorrelation,

$$\int s(t) s(t+\tau) dt \propto \delta(\tau). \qquad (2.6)$$

Carry out a GPR measurement on the surface, $z=0$, of a soil layer situated between $0 \leq x \leq X_{\max}$, $0 \leq z \leq Z_{\max}$, the depth coordinate z pointing downward. At point (x,z) inside the medium, the wave velocity is $c(x,z)$ and the dielectric permittivity is $\varepsilon(x,z)$. Denote the measured wavefield by $y(x,t)$, $0 \leq x \leq X_{\max}$, $0 \leq t \leq T_{\max}$, where t is two-way time. A statistically homogeneous part, $S = X_1 \leq x \leq X_2$, $Z_1 \leq z \leq Z_2 \subseteq 0 \leq x \leq X_{\max}$, and $0 \leq z \leq Z_{\max}$ of the medium with constant radar wave velocity $c(x,Z) \equiv c$ will map into a rectangular window $W = X_1 \leq x \leq X_2$, $T_1 \leq z \leq T_2$ in the georadargram, inside which

$$t = \frac{2z}{c} \qquad (2.7)$$

holds between two-way traveltime and depth. The recorded wave field is $y_{i,j} = y(i\Delta x, j\Delta t)$, where Δt satisfies

$$\Delta t \leq \frac{1}{2f_0} \qquad (2.8)$$

[35], and Δx is radar station spacing. Assume that on the radar display, the pixel size is exactly Δt. Denote in $(x,z) \in S$, the local refractive index by $r_{i,j} = r(i\Delta x, j\Delta z)$, where $\Delta z = c\Delta t/2$. The input radar signal is sampled as $s_i = s(i\Delta t)$, $i = 0, 1, ..., m$, where $m\Delta t$ is signal length. In W, the recorded GPR signature is convolution of the input signal with the series of refractive indices:

$$y(x, j\Delta t) = \sum_{i=0}^{m} s(i\Delta t) r(x, [j-i]\Delta z). \qquad (2.9)$$

With the usual notation $\{y(x, j\Delta t)\} = \{s_j\} * \{r(x, j\Delta z)\}$, where * denotes the convolution, $\{f\} * \{g\}|_j = \sum_i f_i g_{j-i}$.

B. Fractal permittivity distribution implies fractal GPR record

Suppose that in soil section S, the permittivity is bimodal: either $\varepsilon = \varepsilon_{\text{low}} \approx 1$, or $\varepsilon = \varepsilon_{\text{high}} \gg \varepsilon_{\text{low}}$, and that the set of high-permittivity points $S_{\text{permittive}} = \{(x,z) | \varepsilon(x,z) \approx \varepsilon_{\text{high}}\}$ is fractal with the same mass fractal dimension D as the pore set. If $(x,z) \in S$, $(x',z') \in S$, then $\langle \varepsilon(x,z) \varepsilon(x',z') \rangle \propto (\sqrt{(x-x')^2 + (z-z')^2})^{D-2} \propto \langle r(x,z) r(x',z') \rangle$. The following three *propositions* establish exact relations between the fractal dimensions of radargrams and fractal dimensions of the high-permittivity points. (Their proofs are found in the Appendix.)

(a) *Proposition 1. The radar response* $y(x,t)$ *of a soil layer* S *with isotropic fractal permittivity distribution has the same horizontal fractal autocorrelation function* $\langle y(x,t) y(x+\Delta) \rangle \propto \Delta^{D-2}$ *as the permittivity field* $\varepsilon(x,z)$ *has in* S.

(b) *Proposition 2. The radar response $y(x,t)$ of a medium S with isotropic fractal permittivity has the same vertical fractal autocorrelation function $\langle y(x,t)y(x,t+\tau)\rangle \propto \tau^{D-2}$ as the permittivity field has in S. If the permittivity distribution is ergodic, its fractal dimension D can be estimated from almost every single GPR trace of $y(x,t)$.*

(c) *Proposition 3. If we consider the georadargram as a binary image (black corresponding to pores), then the mass fractal dimension of the black pixels in window W is the same as the mass fractal dimension D of the high-permittivity points in S.*

C. Computer simulation of radar wave reflection

The agreement between the mass fractal dimension of the high-permittivity points in the soil, and of the positive amplitudes on the georadargram, has also been verified by numerically solving the wave equation [36]

$$\frac{\partial^2}{\partial z^2}E(x,z)+q^2[\sin^2\theta_0+\varepsilon(x,z)-1]E(z)=0, \quad (2.10)$$

subject to the boundary conditions

$$e_0+e_r=E(0),$$

$$iq\sin\theta_0(e_0-e_r)=\left.\frac{\partial E}{\partial z}\right|_{\forall x,z=0} \quad (2.11)$$

[$q=\omega/c$ is wave number in vacuum; θ_0 is the angle of incidence on the layer from above; $\varepsilon(x,z)$ is complex dielectric permittivity; $E(x,z)$ is the em field inside the medium; $e_0(x)$, and $e_r(x)$ are the reflected and transmitted waves, respectively, and $i=\sqrt{-1}$]. Equations (2.10) and (2.11) were approximated by a symmetric difference equation and solved by the sweep method. Several simulations were run on synthetic shapes with different types of symmetry (Fig. 1), and on microscopic images of the soil (Fig. 2). The binary images were "explored" by simulated em waves, pixel by pixel; and in all cases, good correlation was found between the fractal dimension extracted from the microscopic image and the fractal dimension of the reflected intensity profile $|e_r(x)|$.

III. GEOSYSTEMS DESCRIPTION

Four geosystems of Mexico, in steady- or stationary-state moisture condition, were selected for study. These soils and sediments consist of materials with contrasting morphological and physical properties, and displayed self-similar behavior both in their solid and pore sets from microscopic to macroscopic length scales [37]. A Pulse Ekko model 1000 radar system with 225 MHz antenna was used for the field survey. In order to correlate radar data with geology, a reference section was cut in each site, down to some 1.5–4.0 m depths depending on the estimated penetration of microwaves. By matching these reference sections with the reflectors on the georadargrams, we obtained accurate microwave velocities. The reference sections were also used for soil
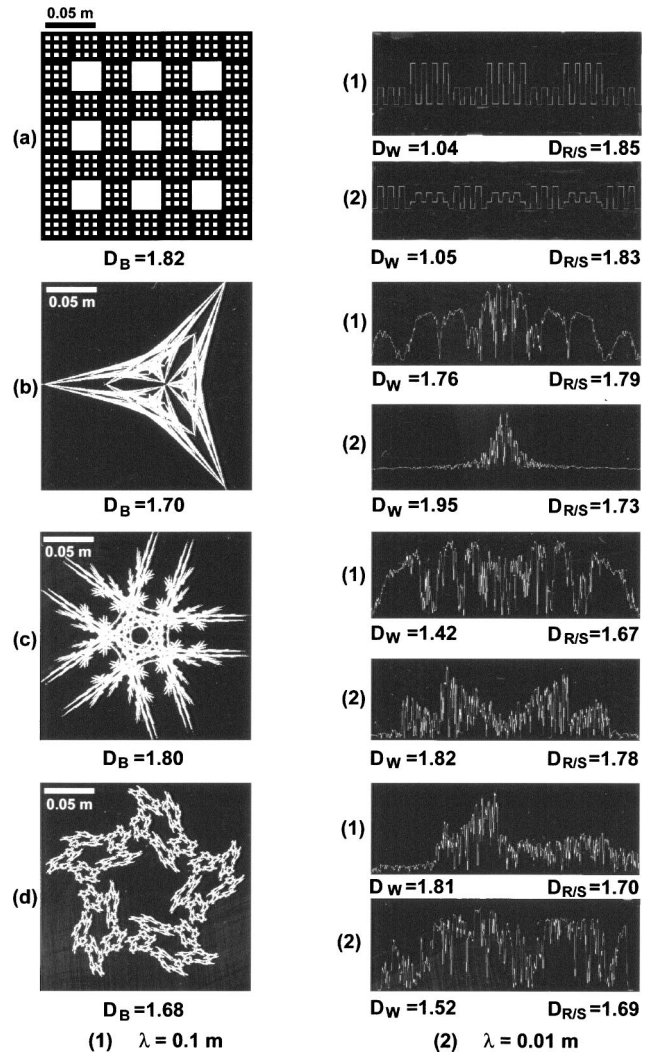

FIG. 1. Simulated radar wave reflection from objects of size 0.2 m with different type of symmetry. The permittivity distribution is (a) a Sierpinski-carpet [21], (b) and (c) nonfractal, (d) synthetic fractal. In each image, white corresponds to $\varepsilon=10$, black to $\varepsilon=1$ permittivities. The superimposed curves show the computed reflected radar intensity $|e_r(x)|$, for $\lambda=0.1$ m (1) and $\lambda=0.01$ m (2) wavelengths. D_B is the box-counting dimension, D_W is the wavelet dimension, and $D_{R/S}$ is the rescaled-range dimension.

morphologic description, micromorphologic sampling, and geophysical measurements.

A. Melanic Andosol, Veracruz state

Andosols are young volcanic soils characterized by high amorphous clay content, less than 0.8 Mg m^{-3} bulk density, higher than 70% porosity, and extremely high solid particle specific surface (250 m^2 g^{-1}) [38]. A moist soil contains about 30% of its volume as solid phase, and 70% as liquid and gas. The characteristic size of microaggregates and micropores is less than 0.25 mm [micro units, Fig. 3(a)]. In the reference section, four horizons were identified by *in situ* measured bulk density. The layer with maximum bulk density (390 kg m^{-3}) has the minimum dielectric constant (18.7). A change in bulk density from 390 to 300 kg m^{-3} coincides
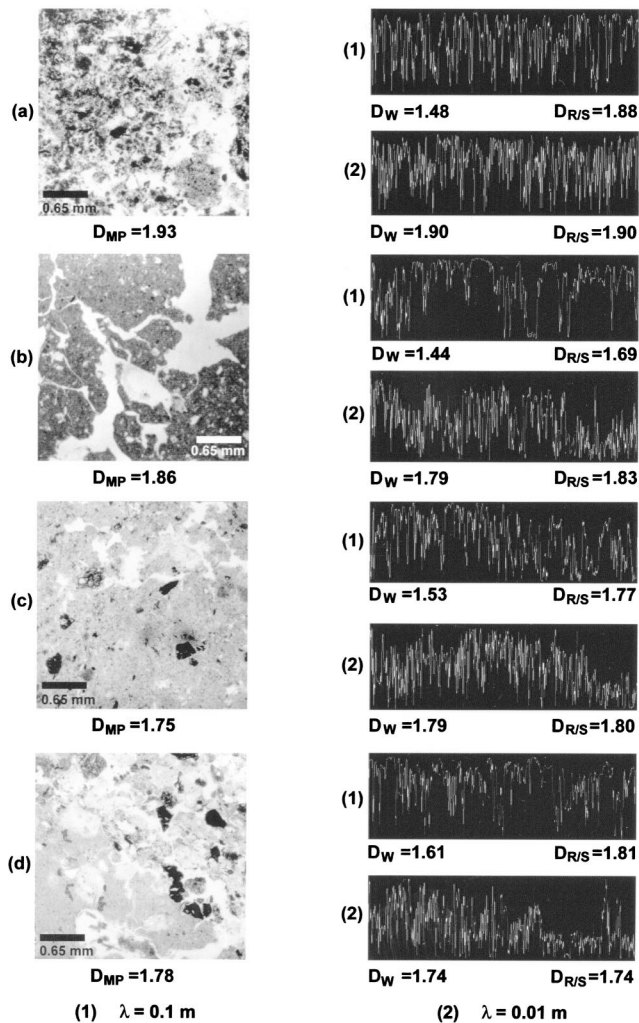
FIG. 2. Simulated radar wave reflection from micromorphologic images of soils, considered as real 0.2 m sized objects: (a) Melanic Andosol, (b) Eutric Vertisol, and (c) and (d) Texcoco Lake deposits. In each image, white corresponds to $\varepsilon = 10$, black to $\varepsilon = 1$ permittivities. The superimposed curve is the computed reflected radar intensity $|e_r(x)|$, for (1) $\lambda = 0.1$ m and (2) $\lambda = 0.01$ m wavelengths. D_{MP} is the pore mass fractal dimension, D_W is the wavelet dimension, and $D_{R/S}$ is the rescaled range dimension.

with a significant increase in water content (from 25.3 to 58.3 %) and dielectric constant (from 18.7 to 44.4).

B. Eutric Vertisol, Guanajuato state

Eutric Vertisol, under continuous drip irrigation, was selected as a typical local agricultural soil, with high shrink-swell capacity, well-developed macrostructure and poorly defined microstructure. Macroaggregates are 25 to 100 mm size [Fig. 3(b)] their stability is especially dependent on the soil's wet-dry cycles. The Vertisol's physical properties vary with moisture content and the associated shrink-swell phenomena. A moist soil would contain about half of its volume as solid phase, the other half shared by liquid and gaseous phases [39]. This proportion drastically changes during dehydration when the bulk density increases from 0.9–1.2 $Mg\,m^{-3}$ to 1.6–2.0 $Mg\,m^{-3}$.
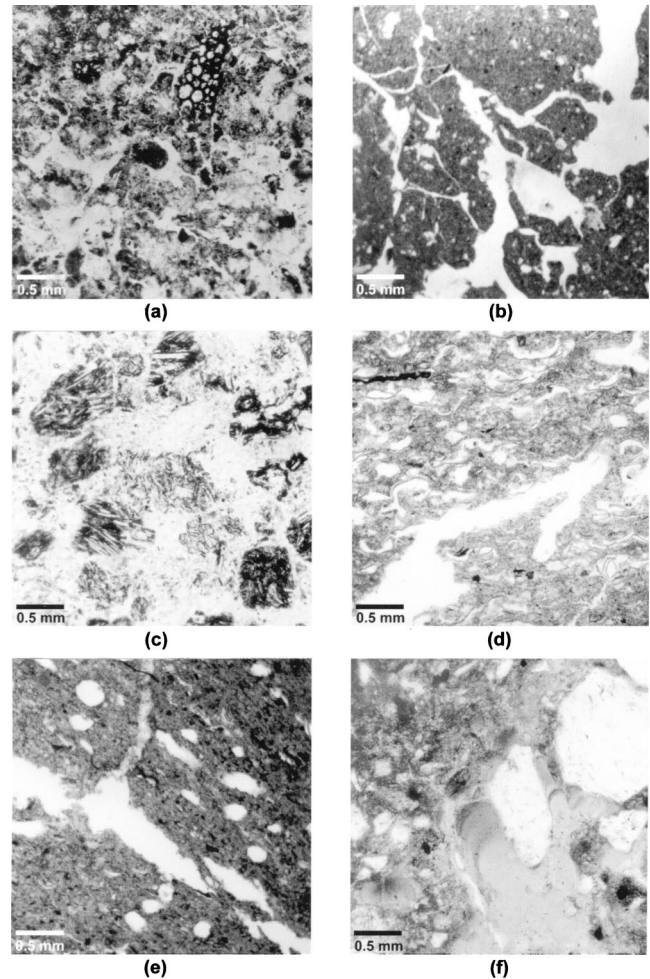

FIG. 3. Microscopic images of the more contrasting horizons of the (a) Melanic Andosol; (b) Eutric Vertisol; (c), (d), and (e) Texcoco lake; (f) Tepetates profile.

Three horizons were distinguished in the reference section by physical measurements. The most important differences are related to the soil's mechanical resistance, which has changed from 797 (0–15 cm) to 1317 $KPa\,cm^{-2}$ (30–45 cm), reflecting the presence of a pass horizon compacted by machine–"plough-pan." The high variabilities of bulk density, volumetric water, and apparent dielectric constant are related to the presence of fissures. The atypical behavior of this soil is well documented [39,40].

C. Texcoco Lake sediments, Mexico state

The moderately well-drained soils had been formed on lacustrine deposits, with exceptionally high water retention capacity: 1 g of clay retains more than 3.5 g of water [41]. The reference section is 1.62 m deep, and is separated into two very contrasting parts by a 30-cm-thick compacted basaltic volcanic ash layer of 1.42 $Mg\,m^{-3}$ bulk density [Fig. 3(c)]. It is overlain by a 39-cm organic-matter-rich layer of around 0.98 $Mg\,m^{-3}$ bulk density. Underlying the volcanic ash layer are lacustrine clay sediments, in direct contact with the water table [Fig. 3(e)] which occurs at 1.8 m depth. The bulk density of clays varied from 0.43 [Fig. 3(d)] to 0.28

$Mg\,m^{-3}$ [Fig. 3(e)]. There are six horizons with clearly different morphology, physical and mechanical properties in this reference section, separated by regular, perfectly horizontal boundaries.

D. Tepetates, Mexico state

In Latin America, hardened soils of volcanic origin are often referred to by vernacular names [42]. In Mexico, these formations are called *Tepetates* which translates as "hard" in the Nahuatl Indian language. In general, tepetates in the Mexican high plateau are natural, massive, compact and hard formations, cemented by different chemical agents, including clays and silica. They are considered barren because of the low connectivity of their pore space [Fig. 3(f)]. Hardness, low hydraulic permeability, and dielectric permittivity (near 3) are their distinctive characteristics. Ten horizons with contrasting properties were described in the reference section. The cemented horizons were separated by clayey layers, some of them being paleosoils [37].

IV. EXPERIMENTAL DESIGN

A. Micromorphologic analysis

At each site, three undisturbed samples (8×4 cm^2) were collected with metal samplers from each layer of the reference section. All samples were taken at field moisture and transported in plastic bags without drying. In the laboratory, samples were dried by acetone replacement (in liquid phase) method and then impregnated with a 1:1 mixture of epoxy resin (HU-543) and acetone [43]. Soil cores were reimpregnated with the same resin under vacuum conditions. When the resin hardened, samples were horizontally sectioned parallel to the soil surface.

Three thin sections (2×4 cm^2, 30 μm average thickness) were prepared from each sample by standard procedure [44] and analyzed under Olympus, BH-2 petrographic microscope. Four black-and-white photographs were taken at the same scale from each thin section. Examples for more contrasting optical microscopy digital images, one for each site, are shown in Figs. 3(a)–3(d).

B. Field survey

The Pulse Ekko model 1000 radar system with antenna of 225 MHz central frequency was used for field surveys. The penetration depths were significantly different in the four sites, fluctuating between 1.50 m in the Vertisol to 4.00 m in the Tepetates. Mean radar wave velocity varied from 0.046 to 0.143 m ns^{-1}, dielectric permittivity changed from 4.4 to 65.9. Assuming a quarter-wavelength resolution, the 225 MHz GPR antenna could resolve objects between 4 to 16 cm size [45–47]. Only those parts of the unprocessed vertical common offset radar profiles that corresponded to the estimated depth of radar penetration [12] were used for fractal analysis.

C. Fractal analysis

Several fractal dimensions are required for the complete description of a fractal system, each having its special sig-

nificance [22]. We used the BENOIT software [48] for fractal analysis. BENOIT analyzes the data by five self-similar and five self-affine techniques [49]. In the self-similar case, the program acts upon two-dimensional bitmap images, and the self-affine methods require a linear array of data. The self-similar methods available in BENOIT can measure the box dimension D_B, mass dimension D_M, information dimension D_I, perimeter-area dimension $D_{P/A}$, and ruler dimension D_R. We used only the first two (D_B and D_M) for fractal analysis of georadargrams and optic microscopy images. Individual GPR traces and computer-simulated reflected waves were analyzed using the self-affine methods in BENOIT. From the five available methods (wavelets, variogram, power spectrum, roughness-length, and R/S) [48], the wavelets and R/S methods proved to be robust.

D. Time-domain reflectometry

Time domain reflectometry (TDR) was used to measure the relative apparent dielectric constant K_a and the volumetric water content θ_i of the soils and sediments. TDR measures the dielectric constant over broad frequency bands, typically between 100 and 1000 MHz [50]. *In situ* K_a measurements were performed at a series of vertical positions in each layers in the four opened sections, and ten measurements along each GPR transect. The mean values of volumetric water content and apparent dielectric constant were determined at every 1 m along the GPR survey line.

V. DISCUSSION

The interaction of waves with fractal media is a complex subject [51,52], where conventional wave equation formalism does not apply because of nondifferentiability. The present study addresses the inverse problem, namely, how to obtain the medium's fractal geometry from the GPR profile?

We analyzed optical microscopy images of the soil, complete GPR profiles and selected parts of them, corresponding to strong reflectors. In all cases, we could demonstrate that the large-scale fractal geometry of the medium—expressed by fractal inhomogeneities in the velocity and permittivity distribution [53]—is inherited in the GPR image. (This is similar to Pentland's [54] finding that a fractally rough surface and the intensity distribution on its photographic image have the same fractal dimension.) A single scale-independent fractal dimension has been found for all sets studied. It was shown that the solid (D_{MS}) and pore (D_{MP}) mass fractal dimensions depend on the soil or sediment genesis and degree of compaction [37]. The range of observed differences in the fractal dimensions of contrasting materials is not always statistically significant.

A. GPR profile interpretation

Reference velocities of radar waves and their range of penetration were estimated from the measured permittivity values. In the Melanic Andosol, the apparent dielectric constant varied from 18.7 in the upper layer (95 cm) to 44.4 (at 130 cm). With 0.068 m ns^{-1} mean velocity, an about 2-m penetration was observed [Fig. 4(a)]. For the Eutric Vertisol,
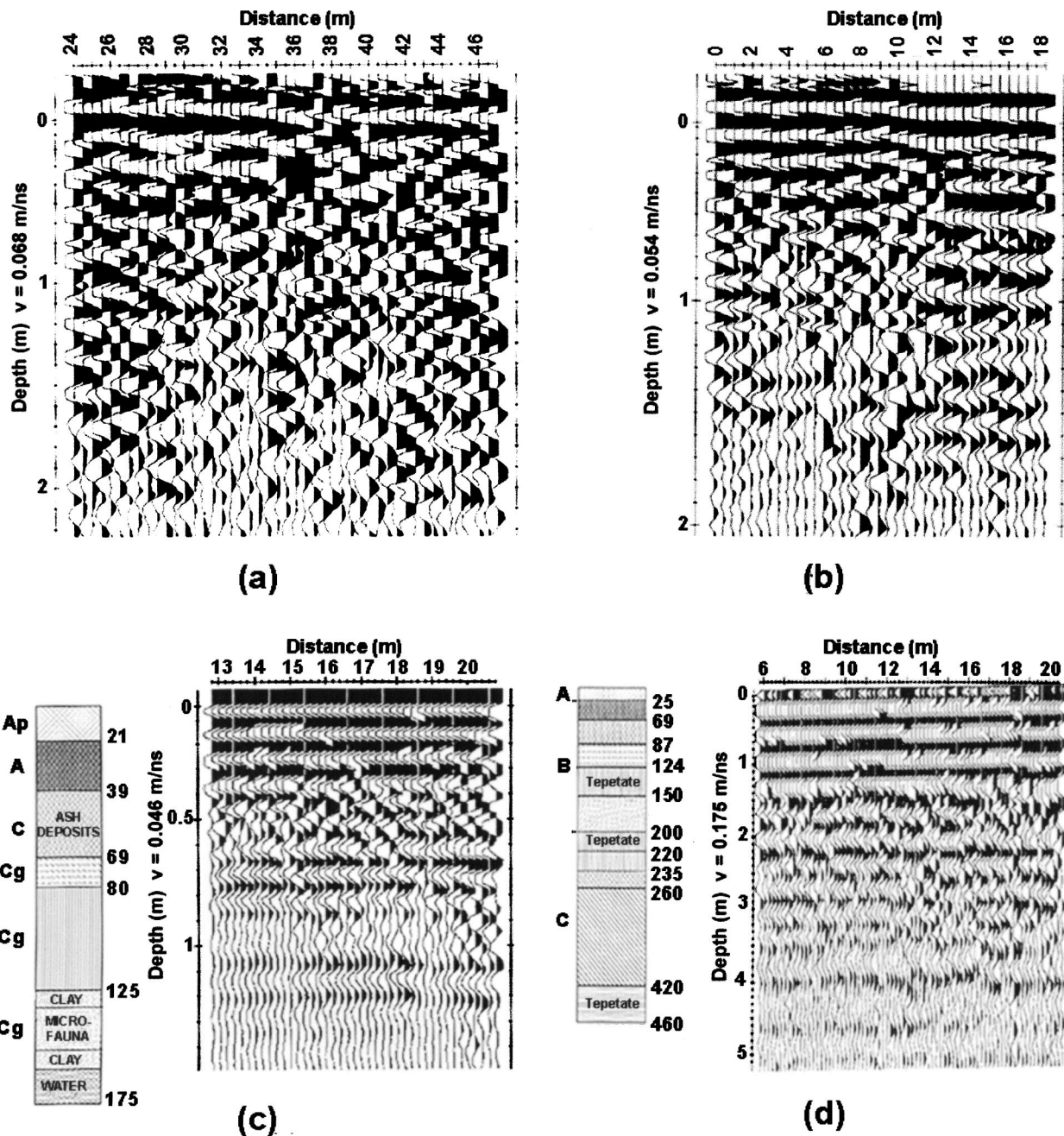
FIG. 4. Common offset georadargrams for (a) Melanic Andosol, (b) Eutric Vertisol, (c) Texcoco Lake, (d) Tepetates profile.

the mean wave velocity was 0.054 m ns^{-1}, depth of penetration was approximately 1.5 m which was the smallest for all compared materials. The first strong reflector (*RI*) related to the plough-plan was detected at near 30 cm depth. The short, inclined, strong reflectors on the Vertisol georadargram are related to the broad and deep fissures in this soil [Fig. 4(b)]. In the Texcoco profile, we found a mean wave velocity of 0.054 m ns^{-1} and 1.8-m penetration [Fig. 4(c)]. The second pair of reflectors (1.2 and 1.4 m depths) coincided with the enrichment of the clay layer with carbonised microfauna bodies (Fig. 5). The largest mean wave velocity (0.143 m ns^{-1}) and deepest penetration ($\approx$4 m) occurred for the Tepetate profile, related to the low mean permittivity (4.4) and quasistate moisture content inside the cemented hori-

zons. Five groups of horizontal reflectors were identified at the reference section: the reflectors at 1.5 and 1.8 m can be related to the lower limit of the $t2a$ tepetate layer (150 cm), those between 2.0 and 3.0 m correspond to the $t2b$ boundaries, and those at 4.0 and 4.5 m are associated with the $t3$ tepetate [Fig. 4(d)]. The first three strong reflectors (0.5, 0.8, and 1.2 m), are related to the fragmented arable horizon of recuperated tepetate.

B. GPR profile fractal analysis

A single scale-independent fractal dimension was found in each compared georadargram. More compact deposits (Tepetates) and materials with submicroscopic porosity (Tex-
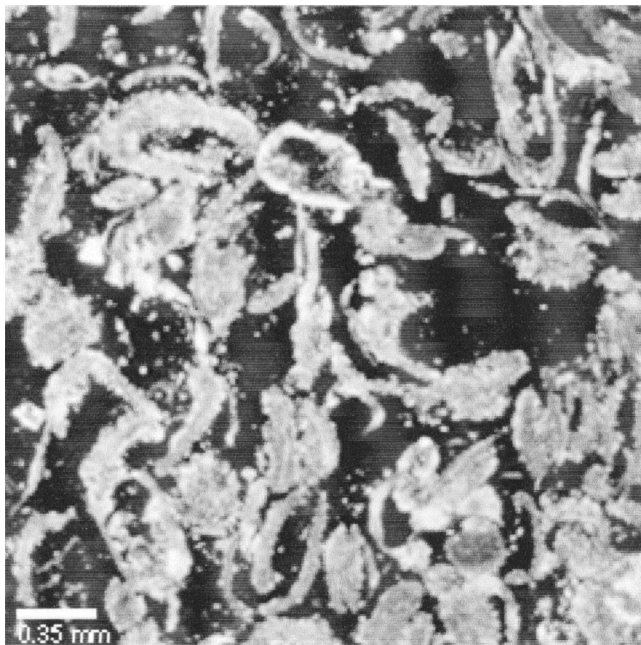
FIG. 5. Microscopic image from the clay horizon, Texcoco Lake profile, with carbonized microfauna bodies (polarized light).

coco Lake) have smaller fractal dimensions D_0, estimated from the georadargram (Table I) and there is good correlation between the D_0 values and the pore network fractal dimensions, estimated on the microscopic images [Fig. 6(a)]. For each site, the fractal dimensions D_0 of the black part of all analyzed georadargrams, are close to the soil pore fractal dimensions D_{MP} and significantly different from the solid network fractal dimensions D_{MS}. There is high correlation ($R^2 = 0.99$) between the mean values of D_0 and D_{MP}, and an inverse tendency between D_0 and D_{MS} [$R^2 = 0.71$, Fig. 6(b)]. The fractal dimensions of the white part of the georadargram (D_{255}) were related to the pore and solid fractal dimensions, respectively, with $R^2 = 0.94$ and $R^2 = 0.73$ [Figs. 6(c) and 6(d)].

When we analyzed separate zones of the georadargrams between coherent reflectors [Figs. 7(a)–7(d)], we got significant linear relations between D_0 and D_{MP} for the more contrasting horizons of Tepetates [$R^2 = 0.99$, Fig. 7(c)] and Texcoco Lake [$R^2 = 0.95$, Fig. 7(b)], and less significant ones in the more homogeneous soils [Figs. 7(a) and 7(d)].

The fractal dimensions of the solid, respectively pore sets, estimated on micromorphologic images and extracted from georadargram have a strong statistical relation with depth. The opposing tendencies, depending on stratigraphy and depositional history, were detected when comparing different soils (Figs. 8 and 9).

The zone-by-zone fractal analysis of the georadargrams has proved the GPR's high resolution and its capacity to

TABLE I. The soil solid (D_{MS}) and pore (D_{MP}) fractal dimensions, extracted from optical micrographs, compared with the fractal dimensions of the georadargrams' black (D_0) and white (D_{255}) part, respectively. (The standard deviation fluctuated between 0.001 and 0.016 for all data.)

| Soil	Microscopic image		Georadargram		GPR profile, between horizons	
	D_{MS}	D_{MP}	D_0	D_{255}	D_0	D_{255}
Melanic Andosol						
mean value	1.930	1.896	1.851	1.937		
(0–50)cm	1.937	1.882			1.842	1.922
50–100	1.925	1.897			1.829	1.879
100–150	1.928	1.908			1.799	1.898
Eutric Vertisol						
mean value	1.937	1.828	1.824	1.945		
0–30	1.931	1.888			1.867	1.892
30–100	1.935	1.727			1.794	1.934
100–150 cm	1.944	1.799			1.776	1.955
Tepetate profile						
mean value	1.964	1.759	1.787	1.950		
0–120	1.955	1.842			1.839	1.914
120–200	1.941	1.777			1.850	1.882
200–235	1.968	1.791			1.809	1.899
260–400	1.965	1.761			1.815	1.942
400–430	1.988	1.622			1.760	1.951
Texcoco Lake						
mean value	1.952	1.771	1.788	1.950		
0–40	1.943	1.843			1.868	1.857
40–80	1.955	1.765			1.763	1.937
80–160	1.967	1.705			1.709	1.977
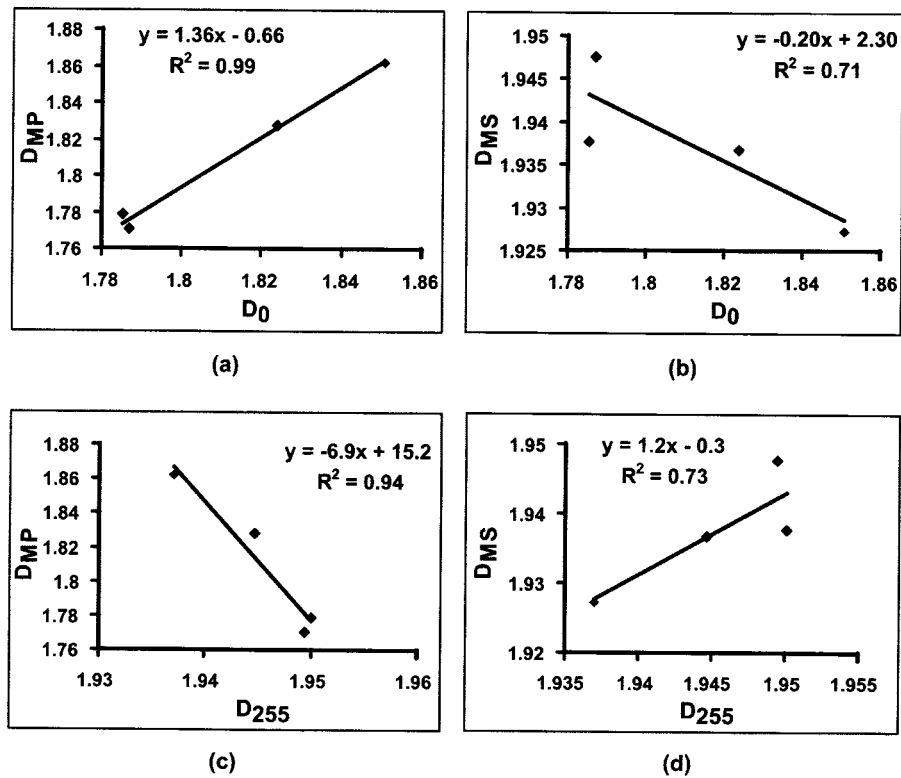
FIG. 6. Fractal dimension D_0 of the georadargram's black part compared with (a) the pore (D_{MP}) and (b) solid (D_{MS}) fractal dimensions; (c) and (d)—the same for the fractal dimension D_{255} of the white part of the georadargram. Only the mean values of fractal dimensions are compared.
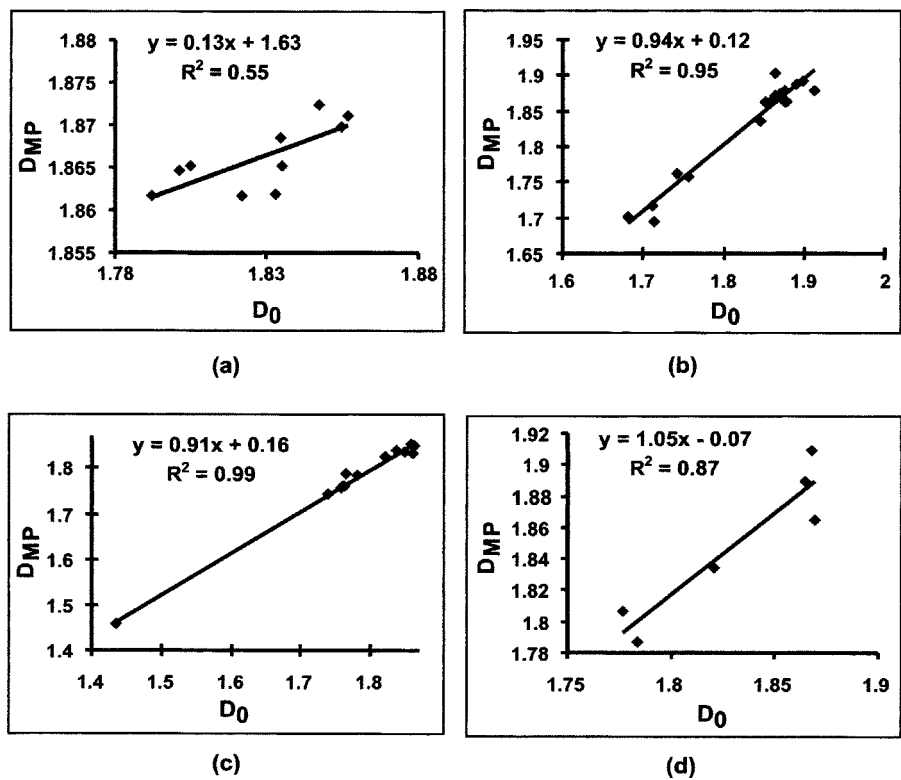

FIG. 7. Fractal dimension D_0 of the georadargram's black part compared with the pore set's fractal dimension (D_{MP}) inside the zones between coherent reflectors: (a) Melanic Andosol, (b) Texcoco Lake, (c) Tepetates profile, and (d) Eutric Vertisol.
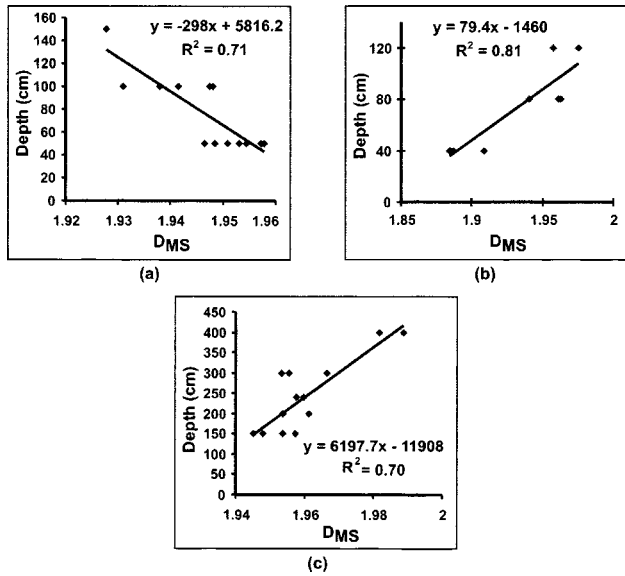
FIG. 8. Change of the solid set's fractal dimension with depth, in (a) Melanic Andosol, (b) Texcoco Lake, and (c) Tepetates profile.

reflect the hierarchic geometry of the pore space. Best results were obtained in profiles with contrasting permittivities (Texcoco Lake and Tepetates, Table I). In the upper part of

the Texcoco Lake profile, the black parts of the georadargram had the highest fractal dimension (1.87), while in the clay horizon (80–160 cm) the smallest (1.71). Both values agreed with the pore fractal dimensions of the same layers (1.87 and 1.70, respectively), but differed from the solid set's fractal dimensions (1.89 and 1.97). The same regularity was observed for the other profiles.

C. GPR trace fractal analysis

Theoretically, it is possible to reconstruct the medium's properties from a single reflected radar trace (Ref. [55], and Proposition 2 of this paper). We analyzed selected individual traces of common offset georadargrams, using self-similar techniques [Figs. 10(a)–10(d)], and then analyzed the complete traces' amplitude distribution, applying self-affine methods [Figs. 11(a)–11(d)]. We called the latter distribution "GPR fractal signature." Both analyses confirmed the fractal nature of the scattered microwaves, and strong correlation was obtained between the fractal dimensions extracted from micromorphologic images, complete georadargrams, individual traces, and amplitude distributions. The mean fractal dimensions calculated for traces were always slightly lower than those estimated from images. This decrease in fractal dimension might be due to signal clipping (Eq. A4.2), or to structural heterogeneity.
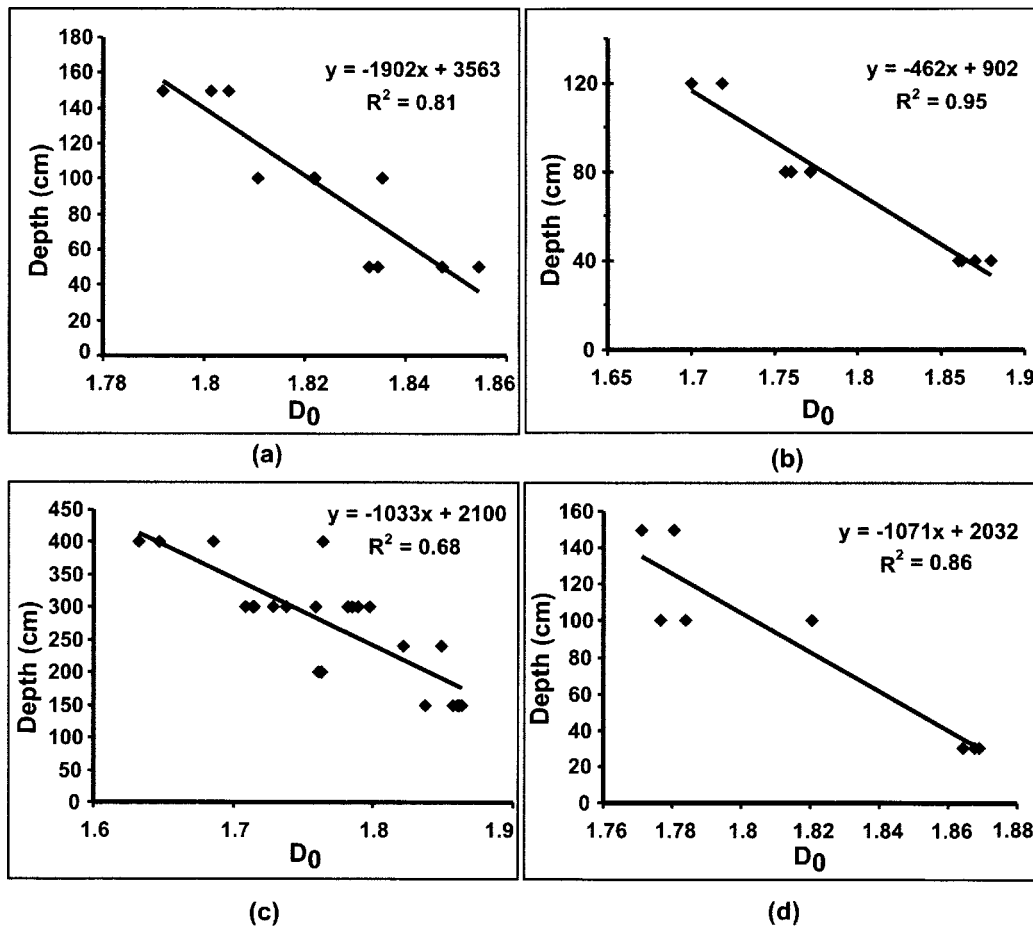

FIG. 9. Fractal dimension D_0 of the georadargram's black part as a function depth in (a) Melanic Andosol, (b) Texcoco Lake, (c) Tepetates profile, and (d) Eutric Vertisol.
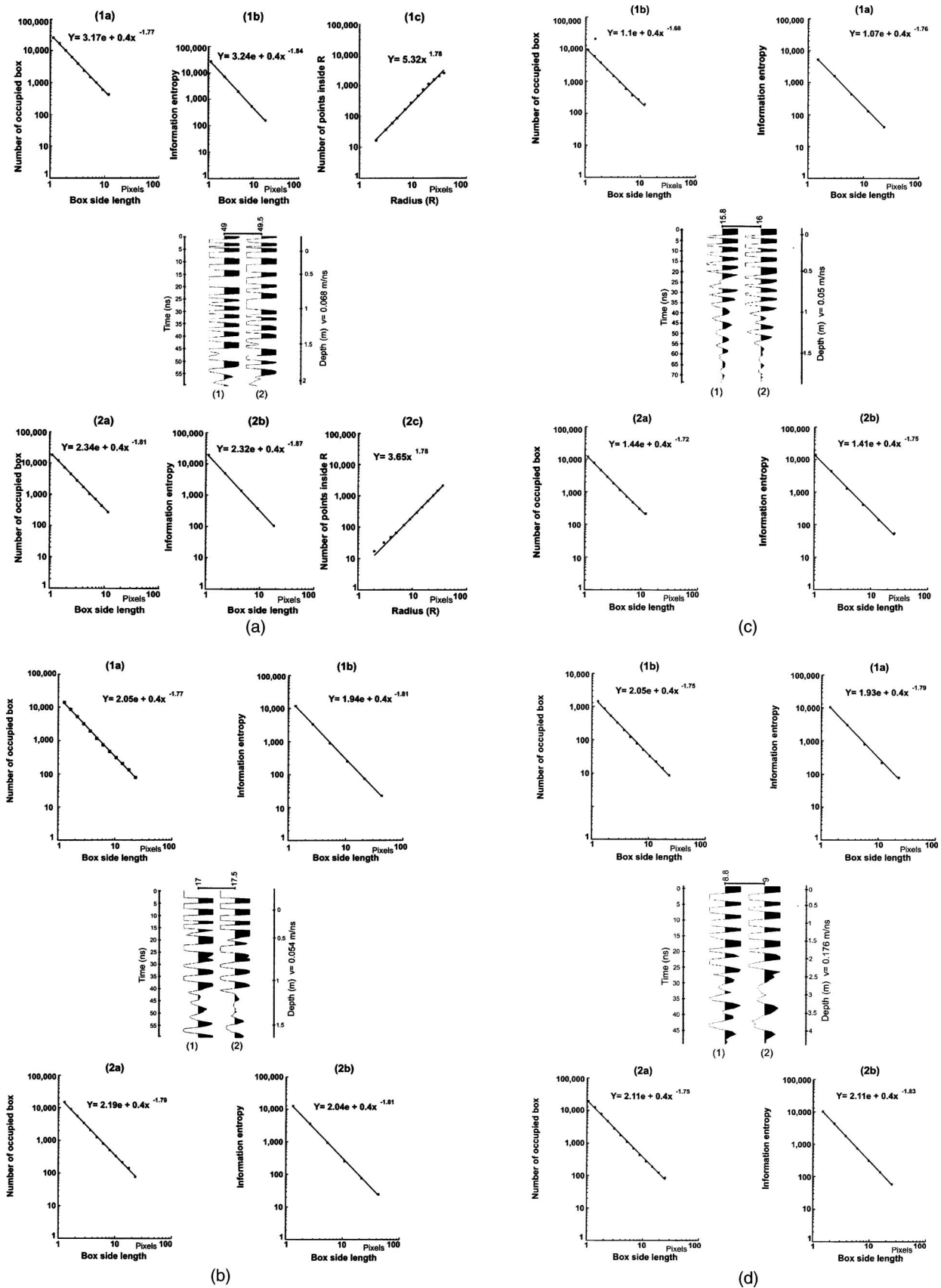
FIG. 10. Self-similar fractal analysis of GPR traces. Examples for box-counting, information entropy estimation, and the mass fractal dimension calculation for the (a) Melanic Andosol, (b) Eutric Vertisol, (c) Texcoco Lake, and (d) Tepetates profile.
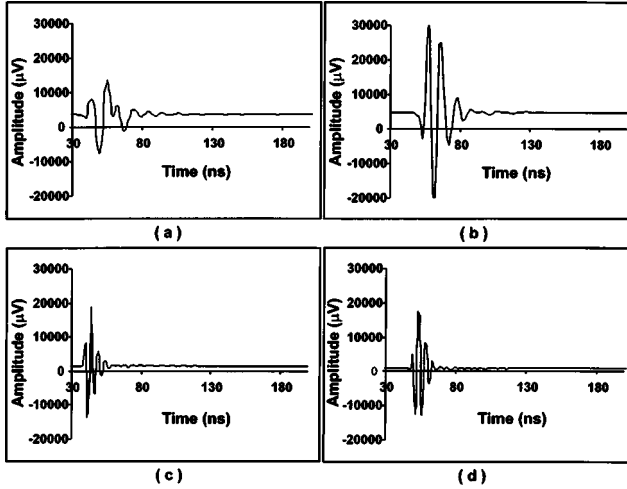
FIG. 11. GPR amplitude distributions ("GPR fractal signature") in (a) Melanic Andosol, (b) Eutric Vertisol, (c) Texcoco Lake, and (d) Tepetates profile.

VI. CONCLUSIONS

We studied experimentally and theoretically the statistics of radar pulses, scattered from fractally heterogeneous soil layers. The ground penetrating radar has produced clear and distinct fractal signatures over four types of soil with contrasting properties. This signature may be directly decoded from the black part of the georadargram, or from the amplitude distribution of the traces. The fractal dimension determined from the georadargram is highly correlated with the fractal dimension of the soil's pore system estimated from microscopic images. It is concluded that the georadargram can be used to reconstruct the fractal structure of the explored media down to the microscopic scale.

APPENDIX: PROOFS OF PROPOSITIONS 1–3

1. Proof of proposition 1

Select two GPR traces from W a distance Δ apart: $y_1(t) = s(t)*r(x,z)$ and $y_2(t) = s(t)*r(x+\Delta,z)$. Denoting by $\{\overline{a_i}\}$, the time-reversal of the series $\{a_i\}$, recalling the commutativity of convolution and that the correlation of a sequence with $\{a_i\}$ is the same as convolving it with its time reversal $\{\overline{a_i}\}$, the expected crosscorrelation between $y_1 = \{y(x,i)\}$ and $y_2 = \{y(x+\Delta,i)\}$ becomes

$$\langle \{y_1\}\{y_2\} \rangle = \langle \{s\}*\{r(x)_j\}*\{\overline{s}\} \circledast \overline{\{r(x+\Delta)_j\}} \rangle$$

$$= [s*\overline{s}]*\langle r(x)_j * \overline{r(x+\Delta)_j} \rangle = R_{ss}(j)*R_{\varepsilon\varepsilon}(\Delta),$$

where the autocorrelation of a random function f is defined as $R_{ff}(\tau) = \langle f(t)f(t+\tau) \rangle$ for functions, and as $R_{ff}(j) = \langle f_i f_{i+j} \rangle$ for time series. As we assumed Eq. (2.6) that $R_{ss}(\tau) = \delta(\tau)$, and as $\delta(t)*f(t) = f(t)$ for any $f(t)$, $\langle y(x,t)y(x+\Delta) \rangle \propto R_{xy}(\Delta) \propto \Delta^{D-2}$.

2. Proof of Proposition 2

Put $y(x,t) = s(t)*r(x,z)$, $y(x,t+\tau) = s(t+\tau)*r(x,z+\zeta)$, and $\zeta = (c/2)\tau$. As in the previous proof $\langle y(x,t)y(x,t+\tau) \rangle = [s(t)*\overline{s(t+\tau)}]*\langle r(x,z)*\overline{r(x,z+\zeta)} \rangle = R_{ss}(\tau)*R_{rr}(\zeta)$. If $R_{ss}(\tau) \propto \delta(\tau)$, $\langle y(x,t)y(x,t+\tau) \rangle \propto \tau^{D-2} = (2/c\zeta)^{D-2} \propto \zeta^{D-2} \propto R_{rr}(\zeta) \propto R_{\varepsilon\varepsilon}(\zeta)$. If the permittivity distribution $\varepsilon(x,t)$ is ergodic in S [56], $R_{ss}(\tau)$ (and consequently, the mass fractal dimension D) can be estimated from almost every georadargram trace.

3. Proof of Proposition 3

Consider the georadargram as a binary image, and analyze an $(N \times N)$-size square in it, where N is in pixel-size units. Let this square correspond to some rectangular $(L \times Z)$-size domain in the geologic section, inside which c is constant and the local permittivity maxima are distributed as a mass fractal with dimension D. Let, on the display, the distance between traces be A_{max}[pixels], while the real distance between radar stations is Δx. Suppose that the graph of a single elementary signal reflected from an isolated high-permittivity scatterer contains altogether B black pixels. Then

$$L = \frac{N[\text{pixel}]}{A_{max}[\text{pixel}]}\Delta x = A \cdot N;$$

$$Z = N[\text{pixel}]\Delta t \left[\frac{\sec}{\text{pixel}}\right]\frac{c[\text{m/s}]}{2} = B \cdot N. \qquad (\text{A3.1})$$

Estimate the total number of black pixels in the $(N \times N)$-size georadargram window. Under any radar station, there are $\propto Z^{D/2} \propto N^{D/2}$ high-permittivity scatterers (i.e., pores—the exponent $D/2$ follows from the generalized Delesse's principle [57]). These contribute $\propto \mu B N^{D/2} \propto N^{D/2}$ black pixels to the corresponding trace. Here $0 < \mu < 1$ is a constant to compensate for the losses of black pixels in cases when positive parts of a reflected signal $s(t-\tau_1)$ are destructively interfering with negative parts of an other wave $s(t-\tau_2)$. (If the arrival-time distribution is Poisson, μ can be estimated from Campbell's theorem [35].) A similar reasoning shows that along a randomly selected horizontal row of the selected georadargram window, there are $\propto N^{D/2}$ black pixels. By [57] the total number of black pixels in the $(N \times N)$-sized georadargram window scales as $\propto N^{D/2}N^{D/2} \propto N^D$; that is, in any part of the georadargram corresponding to a homogeneous soil section, the black pixels form a fractal set with the same mass fractal dimension as the high-permittivity points in the soil.

4. The effect of signal clipping

We assumed in Proposition 3 that the display gain and spacing between trace centers have been set to avoid clipping. Still, in practice, some clipping always arises (Fig. 10). We have checked experimentally that if the large amplitudes are only slightly clipped, the fractal dimension of the trace is preserved. In the other extreme, the signature becomes a telegraph signal [35] with exponential autocorrelation $R \propto e^{-\lambda|\tau|}$, where λ is the Poisson density of wave arrivals. By Eqs. (2.4) and (A4.2) $\lambda = \alpha|\tau|^{D-2}$, where α is constant, that is $R \propto e^{-\alpha|r|^{D-1}}$. If the autocorrelation function of a stochastic process satisfies

$$\gamma = \frac{1}{2} \lim_{r \to 0} \frac{\ln[R(0) - R(\tau)]}{\ln \tau} < 1, \qquad (A4.1)$$

then the process is fractal of dimension $2 - \gamma$ [58]. In our case $\gamma = (D-1)/2 < 1$; that is, the extremely clipped trace is still fractal, but its fractal dimension

$$D_{\text{clipped}} = \frac{5 - D}{2} \qquad (A4.2)$$

is less than D if $D \geq 5/3$.

[1] E. Jakeman, in *Fractals in Physics*, edited by L. Pietronero and E. Tosatti (Elsevier Sciences, Amsterdam, 1986), pp. 55–60.

[2] D. L. Jaggard, A. D. Jaggard, and P. V. Frangos, in *Frontiers in Electromagnetics*, edited by D. H. Werner and R. Mittra (IEEE Press, New York, 2000), pp. 1–47.

[3] K. Holliger, Geophys. J. Int. **128**, 65 (1997).

[4] Ch.-A. Guérin and M. Holschneider, J. Phys. A **29**, 7651 (1996).

[5] A. P. Radlinski *et al.*, Phys. Rev. Lett. **82**, 3078 (1999).

[6] C. Allain and M. Cloitre, in *Fractals in Physics*, edited by L. Pietronero and E. Tosatti (Elsevier Sciences, Amsterdam, 1986), pp. 61–64.

[7] P. W. Schmidt, J. Appl. Crystallogr. **24**, 414 (1991).

[8] E. M. Ortiz, F. Gonzalez, and F. Moreno, in *Light Scattering from Microstructures*, edited by F. Moreno and F. Gonzales (Springer, Berlin, 2000).

[9] Ch.-A. Guérin, M. Holschneider, and M. Saillard, Waves Random Media **7**, 331 (1997).

[10] S. K. Sinha, Physica D **38**, 310 (1989).

[11] N. Olivi-Tran *et al.*, J. Phys. B **31**, 4467 (1998).

[12] V. V. Zosimov and L. M. Lyamshev, Phys. Usp. **38**, 347 (1995).

[13] M. V. Berry, in *Structural Stability in Physics*, edited by W. Guttinger and H. Eikemeier (Springer, Heidelberg, 1979), pp. 43–50; M. V. Berry, J. Phys. A **14**, 3101 (1981).

[14] I. D. Simonsen, D. Vandembroucq, and S. Roux, J. Opt. Soc. Am. A **18**, 1101 (2001).

[15] K. Vasudevan, Q. Li, and F. A. Cook, Geol. Rundsch. **85**, 44 (1996).

[16] P. Ulriksen, Ph.D. thesis, Lund University Techn., Sweden, 1982 (unpublished).

[17] D. Goodman, Geophysics **59**, 224 (1994).

[18] K. Oleschko *et al.*, Soil Technology **10**, 207 (1997); K. Oleschko *et al.*, *ibid.* **183**, 1 (1997); K. Oleschko, Soil and Till. Res. **49**, 255 (1998); **52**, 247 (1999); K. Oleschko *et al.*, Soil and Till. Res. **55**, 43 (2000).

[19] M. V. Berry, in *Structural Stability in Physics*, edited by W. Guttinger and H. Eikemeier (Springer, Heidelberg, 1979), pp. 43–50; M. V. Berry, J. Phys. A **14**, 3101 (1981); Ch.-A. Guérin and M. Holschneider, J. Math. Phys. **39**, 4165 (1998).

[20] B. R. Hunt, Proc. Am. Math. Soc. **126**, 791 (1998).

[21] B. B. Mandelbrot, *The Fractal Geometry of Nature* (Freeman, New York, 1983).

[22] G. Korvin, *Fractal Models in the Earth Sciences* (Elsevier, Amsterdam, 1992).

[23] D. L. Turcotte, *Fractals and Chaos in Geology and Geophysics* (Cambridge University Press, Cambridge, 1992).

[24] H. H. Hardy and R. A. Beier, *Fractals in Reservoir Engineering* (World Scientific, Singapore, 1994).

[25] See pp. 273–275 in Ref. [22].

[26] J. P. Hansen and A. T. Skjeltorp, Phys. Rev. **38**, 2635 (1988).

[27] M. Pilkington, M. E. Gregotski, and D. Todoeschuck, Geol. Ryndsch. **42**, 677 (1994).

[28] S. Leonardi and H.-J. Kümpel, IRE Trans. Audio **85**, 50 (1996).

[29] S. Maus, D. Gordon, and D. Fairhead, Geophys. J. Int. **129**, 163 (1997).

[30] S. Zhou and H. Thybo, Pure Appl. Geophys. **151**, 147 (1998).

[31] L. N. Vasil'yev and A. S. Tyuflin, Map. Sci. Remote Sens. **30**, 205 (1993).

[32] G. Korvin, D. M. Boyd, and R. O'Dowd Geophys. J. Int. **100**, 535 (1990).

[33] V. P. Dimri, Geophysics **63**, 1943 (1998).

[34] G. Turner and A. F. Siggins, Geophysics **59**, 1192 (1994).

[35] S. M. Rytov, *Statistical Radio Physics* (Nauka, Moscow, 1966).

[36] A. V. Andreev and R. V. Khachaturov, Repts. Appl. Maths. Computational Center of Russian Ac. Sci., Moscow (1996); A. A. Samarskii, *The Theory of Difference Schemes* (Nauka, Moscow, 1989).

[37] K. Oleschko *et al.*, Soil and Till. Res. **55**, 43 (2000).

[38] B. P. Warkentin and T. Maeda, in *Soils With Variable Charge*, edited by B. K. G. Theng (Palmerston North, New Zealand, 1980).

[39] C. E. Coulombe, L. P. Wilding, and J. B. Dixon, J. Advances Agronomy **57**, 289 (1996).

[40] K. Oleschko, J. D. Etchevers, B. Hernandez, and A. R. Hernandez, Soil and Till. Res. **37**, 15 (1996).

[41] C. Gutiérrez, Ph.D. thesis, Colegio de Postgraduados, Montecillos, Mexico, 1997 (unpublished).

[42] C. Zebrowski, Terra (Mexico) **10**, 15 (1992).

[43] C. P. Murphy, *Thin Section Preparation of Soils and Sediments* (AB Academic Publishers, Great Britain, 1986).

[44] R. Brewer, *Fabric and Mineral Analysis of Soils* (R. E. Krieger, Huntington, 1964).

[45] M. J. Friedel, J. A. Jessop, and R. E. Thill, U.S. De-

partment of the Interior, Bureau of Mines Report of Investigations 9424, 1992 (unpublished).

[46] G. Grandjean, G., and J. C. Gourry, J. Appl. Geophys. **36**, 19 (1996).

[47] J. A. Doolittle and M. E. Collins, J. Appl. Geophys **33**, 101 (1995).

[48] See, http//www.scioncorp.com

[49] W. Seffens, Science **285**, 1228 (1999).

[50] F. N. Dalton and M. Th. van Genuchten, Geoderma **38**, 237 (1986); G. C. Topp, J. L. Davis, and A. P. Annan, Water Resour. Res. **16**, 574 (1980).

[51] J. A. Hudson, Geophys. J. R. Astron. Soc. **69**, 649 (1982); I. Lerche, Pure Appl. Geophys. **123**, 503 (1985); R. S. Wu and K. Aki, *ibid.* **123**, 805 (1985).

[52] J. R. Bohavar, J. R. and J. F. Willemsen, Phys. Rev. B **30**, 6778 (1984); A. E. Dubinov, and V. D. Selemir, in *Fractals in Ap-plied Physics*, edited by A. E. Dubinov (Arzamas, Russia, 1995); D. Noskov and A. V. Shapovalov, Ser. Phys. **7**, 120 (1993); I. M. Sokolov, Usp Fiz. Nauk **150**, 221 (1986).

[53] J. M. Carcione, Geophysics **61**, 1664 (1996).

[54] A. P. Pentland, IEEE Trans. Pattern Anal. Mach. Intell. **6**, 661 (1984).

[55] M. L. Vladov and A. V. Starovoitov, *Georadiolocation Studies of the Profile's Top Part* (Moscow State University, Russia, 1999).

[56] L. A. Chernov, *Wave Propagation in Random Media* (McGraw-Hill, New York, 1960).

[57] K. Oleschko, Soil and Till. Res. **49**, 255 (1998); **52**, 247 (1999).

[58] S. I. Denisov, Chaos, Solitons Fractals **9**, 1491 (1998); D. A. Rothrock and A. S. Thorndike, J. Geophys. Res. **85**, 3955 (1980).